

# Chimeras in digital phase-locked loops

Bishwajit Paul<sup>1</sup> and Tanmoy Banerjee<sup>1, a)</sup>

*Chaos and Complex Systems Research Laboratory, Department of Physics, University of Burdwan, Burdwan 713 104, West Bengal, India.*

(Dated: 15 December 2024; Received :to be included by reviewer)

Digital phase-locked loops (DPLLs) are nonlinear feedback-controlled systems that are widely used in electronic communication and signal processing systems. In most of the applications they work in coupled mode, however, vast of the studies on DPLLs concentrate on the dynamics of a single isolated unit. In this paper we consider both one- and two-dimensional array of DPLLs connected through a practically realistic nonlocal coupling and explore their collective dynamics. For the one-dimensional array we analytically derive the parametric zone of stable phase-locked state in which DPLLs essentially work in their normal mode of operation. We numerically demonstrate that apart from the stable phase-locked state, a large number of spatiotemporal structures including chimeras arise in a broad parameter zone. For the two-dimensional array under nonlocal coupling we identify several variants of chimera patterns, such as grid and strip chimeras. We identify and characterize the chimera patterns through suitable measures like local curvature and correlation function. Our study reveals the existence of chimeras in a widely used engineering system, therefore, we believe that these chimera patterns can be observed in experiments also.

PACS numbers: 05.45.Xt, 05.45.Gg, 05.45.Pq

Keywords: digital phase-locked loop, non-local coupling, chimera, 2D-array.

The phase locking is an intriguing phenomenon observed in the field of physics, biology and engineering. Based on the technique of phase locking de Bellescize invented the phase-locked loop (PLL) in 1932, which has been in the heart of the electronic communication system and signal processing. Starting from the analog television receivers in the late thirties of the previous century, PLLs are now a days used in applications, such as hard-disk drives, modems and atomic force microscopy. With the advent of digital IC technology, PLLs are rapidly replaced by their digital counterpart, namely the digital phase-locked loops (DPLLs). In the initial years, a single unit of DPLL was sufficient for a particular application. However, modern communication systems demand networking and parallel processing, and therefore, DPLLs typically have to work in cascade. Being a nonlinear system, a vast amount of studies have been dedicated to understand the dynamics of a single DPLL, however, only a few studies are available on networks of coupled DPLLs. In general, the dynamics of coupled systems are complex and challenging to understand, especially with the discovery of new spatiotemporal patterns, like chimera states.

This paper deals with the coupled dynamics of DPLLs and reports the occurrence of chimeras in the one- and two-dimensional network of DPLLs under the practical coupling scheme. We show that apart from the stable phase-locked state, which is essential for the normal operation of

DPLLs, the networks show several chimera patterns in a broad parameter space. Our study is significant in the sense that it established the presence of chimeras in a widely used engineering system.

## I. INTRODUCTION

The phenomenon of phase locking has been fascinating the researchers in the field of physics, biology and engineering. In the field of engineering, based on the technique of phase locking, phase-locked loop (PLL) was invented<sup>1</sup>, which, along with its digital counterpart, the digital phase-locked loops (DPLLs), are essential units of electronic communication and signal processing systems. DPLLs are nonlinear discrete feedback-controlled systems that have wide applications in integrated electronic devices and coherent communication systems<sup>1,2</sup>. They are used in the receiver segment of a communication system as data-clock recovery circuit and frequency demodulators. Also, they are an important part of various electronic systems such as digital signal processors and hard-disk drives<sup>3</sup>. Apart from their application potentials, DPLLs (and PLLs) exhibit rich complex phenomena such as bifurcations and chaos<sup>4</sup>, which has widely been studied in the literature.

In modern applications, typically DPLLs work in cascade, i.e., they operate under coupled condition. Take for instance the problem of clock skew in clock synchronizers of a multiprocessor system under the application of parallel processing where the units are spatially separated<sup>5</sup>. In this system it is absolutely necessary to use PLLs in coupled mode to synchronize the units (and to avoid clock

<sup>a)</sup> Electronic mail: tbanerjee@phys.buruniv.ac.in

skew). Therefore it is important to understand the collective behavior of an array of coupled DPLLs. However, surprisingly, in the literature only a few studies deal with the coupled behavior of DPLLs: The temporal behavior of two coupled DPLLs was studied in Ref. 6; Goldsztein and Strogatz<sup>7</sup> treated coupled DPLLs as pulse coupled oscillators and derived explicit formulas for the transient time to lock, stability of the synchronized state, and the period of the bifurcating solution at the onset of instability. The collective dynamics of a network of DPLLs with *nearest neighbor coupling* topology has recently been reported by the present authors<sup>8,9</sup>: it was shown that the network depicts the formation of a variety of spatial and spatiotemporal patterns like frozen random pattern, pattern selection, spatiotemporal intermittency and spatiotemporal chaos.

In a real network of spatially separated DPLLs local coupling is weaker to achieve synchronization as the effective coupling strength is typically too weak to overcome the disorder caused by the local dynamics. On the other hand, although global coupling is conducive to synchronization, however, this form of coupling is very massive, costly and complicated to implement in a real network. In this context, the nonlocal coupling topology is the most general one: depending upon the goal of the network one can make a trade-off between the coupling range and the coupling strength. Furthermore, dimensionality of a network also plays crucial role in determining the dynamics. In comparison with the one-dimensional topology, studies on the dynamics of two-dimensional network of oscillators are more general yet relatively less explored in the context of coupled oscillators. In the case of a DPLL based network, a *two-dimensional array with non-local coupling topology* is a much realistic network structure, however, hitherto the dynamics of one- and two-dimensional network of DPLLs with nonlocal coupling has not been studied.

Unlike local coupling<sup>8,9</sup>, it is expected that a nonlocal coupling gives rise to much more complex spatiotemporal behaviors, such as chimera patterns, which is in the center of recent research. The chimera state, discovered by Kuramoto and Bottogtokh<sup>10</sup>, is defined as the hybrid dynamical spatiotemporal state of a network in which different subsets of identical oscillators spontaneously divided into two groups, namely, synchronized (coherent) and desynchronized (incoherent) groups. In the initial years most of the studies explored chimera states in one-dimensional network (see the reviews on chimera Ref. 11 and Ref. 12), however, recent studies reveal many interesting chimera patterns in two-dimensional<sup>13,14</sup> and three-dimensional networks<sup>15</sup>. The current interest on the chimera state can be attributed to its possible connection with the unihemispheric slow-wave sleep of some migratory birds and aquatic mammals<sup>16,17</sup>. The robustness of chimera states are evidenced from their observation in real experimental set up with the optical<sup>18</sup> and chemical<sup>19,20</sup>, optoelectronic systems<sup>21</sup>, and mechanical systems<sup>22,23</sup>. The real world systems also depicts chimera

state e.g., power grids<sup>24</sup>, social networks<sup>25</sup>, and SQUID metamaterials<sup>26</sup> to name a few.

In most of the studies on chimeras the main goal was to wishfully observe chimera in man made systems under certain coupling and initial conditions: however, bulk of the systems under study are of rare practical interest (except in a few systems, such as the occurrence of chimera state in power grids<sup>24</sup> and social networks<sup>25</sup>). Therefore, it is a natural question to ask, whether a real engineering system with wide application like DPLL can show chimera state under its *normal* coupling condition.

Motivated by the above discussion, in this paper we study the dynamics of nonlocally coupled DPLLs in one- and two-dimensional networks. In both the cases depending upon coupling and local dynamics we show that several chimera patterns emerge. For the 1D case we analytically obtain the condition for the phase-locked state, which is the normal and essential mode of operation for DPLLs. In the case of two-dimensional (2D) network we observe several interesting 2D chimera patterns, such as grid and strip chimeras. We characterize the chimera states using quantitative measures such as the local curvature and local correlation function. Finally we also discuss the importance of our study.

## II. SYSTEM DESCRIPTION AND MATHEMATICAL MODEL

### A. Isolated ZC1-DPLL

The functional block diagram of a ZC1-DPLL is shown in the Fig. 1. It consists of a sample and hold block, a digital filter (DF) and a digital-controlled oscillator (DCO). Let us assume that a noise free ( $n(t) = 0$ ) sinusoidal incoming signal  $e(t) = A_0 \sin(\omega_i t + \theta_0)$  is fed to the sample and hold block. Here  $A_0$  being the amplitude,  $\omega_i$  is the angular frequency and  $\theta_0$  be the initial phase of the incoming signal. This signal is sampled by the sample and hold block at each positive going zero-crossing edges of the DCO. The sampled signal  $x_k = e(t_k)$  at the  $k^{th}$  sampling instant  $t_k$  is modified by the DF that in turn generate digital pulses  $y_k$ . This pulse then drive the DCO to determine the next sampling instant of the sample and hold block. The incoming signal  $e(t)$  may be rewritten in terms of the nominal free running angular frequency of the DCO,  $\omega_0$ , as

$$e(t) = A_0 \sin(\omega_0 t + \theta(t)) = A_0 \sin(\phi(t)), \quad (1)$$

where  $\theta(t) = (\omega_i - \omega_0)t + \theta_0$ . Now if we denote the successive sampling instants by  $t_k, t_{k+1}, \dots$ , then the instantaneous time period of the DCO at  $k^{th}$  instant is determined by  $T_k = t_k - t_{k-1}$ . The sequence of samples  $\{x_k\}$  generate control sequences  $\{y_k\}$  that are employed to determine the successive time period by the algorithm<sup>27</sup>:  $T_{k+1} = T - y_k$ , where  $T (= 2\pi/\omega_0)$  corresponds to the nominal period of the DCO. There is no loss of generality if we assume  $t_0 = 0$ <sup>28</sup>; then the sampling instants are

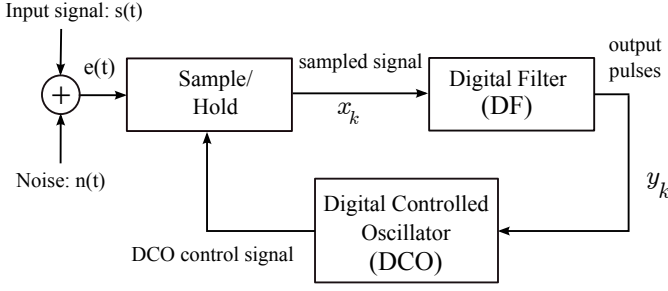


FIG. 1. The figure shows the block diagram of an isolated ZC1-DPLL.

given by

$$t_k = kT - \sum_{i=0}^{k-1} y_i \quad (2)$$

The phase error of the incoming signal in Eq. 1 at the  $k^{\text{th}}$  sampling instant is  $\phi_k = \phi(t_k) = \omega_0 t_k + \theta(t_k) = \omega_0 t_k + \theta_k$ ; then using Eq. (2) we get

$$\phi_k = \omega_0 \left( kT_0 - \sum_{i=0}^{k-1} y_i \right) + \theta_k \quad (3)$$

The first term  $\omega_0 kT_0$  is integral multiple of  $2\pi$  and the effective residual phase error becomes

$$\phi_k = \theta_k - \omega_0 \sum_{i=0}^{k-1} y_i \quad (4)$$

For first-order ZC1-DPLL the digital filter is of a zeroth order filter with no memory element. So the transfer function of such filter is a constant gain element given by  $G_0$  (say). Therefore, the control signal is given by  $y_k = G_0 x_k$ . Then from Eq. (4) one can get the phase error equation as

$$\phi_{k+1} = \Lambda_0 + \phi_k - K_1 \xi \sin(\phi_k) \quad (5)$$

Where  $\xi = \omega_i/\omega_0$  is the normalized incoming frequency,  $\Lambda_0 = 2\pi(\xi - 1)$  and  $K_1 = A_0\omega_0 G_0$ .  $K_1$  is called closed loop gain of the ZC1-DPLL. Physically all  $\{\phi_k\}$ s are modulo  $2\pi$  quantity that are bounded in the interval  $[-\pi : \pi]$ . The Eq (5) is called the system equation of an isolated ZC1-DPLL.

## B. One-dimensional network of ZC1-DPLLs with nonlocal coupling

We consider a one-dimensional (1D) network of nonlocally coupled  $N$  identical ZC1-DPLLs arranged in a ring topology with periodic boundary condition. Figure 2(a) shows the representative sketch of the coupling scheme. The practical coupling architecture in

which a network of coupled ZC1-DPLLs normally works is shown in Fig. 2(b). According to this scheme the  $i^{\text{th}}$  node is coupled with  $R$  nearest neighbors on either side of its position with a normalized coupling strength  $\frac{\epsilon}{2R}$ . The sampled input signal for the  $i^{\text{th}}$  ZC1-DPLL is given by  $x_k^i$ , where the spatial position of this ZC1-DPLL is indexed by the superscript  $i$  and the temporal instant is indexed by a subscript  $k$ . The spatial index  $i$  may have any integral value within the range  $[1 : N]$ . The coupling scheme can be realized by using a weighted adder, that add the sampled signals  $x_k^{i-R}, x_k^{i-R+1}, \dots, x_k^{i-1}, x_k^{i+1}, \dots, x_k^{i+R-1}, x_k^{i+R}$  obtained from the outputs of the sample/hold blocks of respective ZC1-DPLLs. Therefore, the input of the digital filter of the  $i^{\text{th}}$  ZC1-DPLL is given by

$$Z_k^i = x_k^i - \frac{\epsilon}{2R} \sum_{j=i-R}^{i+R} (x_k^j - x_k^i). \quad (6)$$

The second term in the bracket discards the contribution due to the self-feedback. Now the output of the digital filter is given by  $y_k^i = G_0 Z_k^i$ . Here  $G_0$  is the gain constant of the digital filters. We can use the same arguments like an isolated ZC1-DPLL that in turn gives the system equation of the nonlocally coupled ZC1-DPLLs as

$$\begin{aligned} \phi_{k+1}^i &= \Lambda_0 + \phi_k^i - \xi K_1 \sin \phi_k^i \\ &+ \frac{\epsilon \xi K_1}{2R} \sum_{j=i-R}^{i+R} [\sin(\phi_k^j) - \sin(\phi_k^i)]. \end{aligned} \quad (7)$$

Since  $R$  represents the range of nonlocal coupling, therefore, for  $R = 0$ , the network is an ensemble of  $N$  isolated ZC1-DPLLs, whereas  $R = 1$  corresponds to the nearest neighbor coupling. On the other hand if total number of

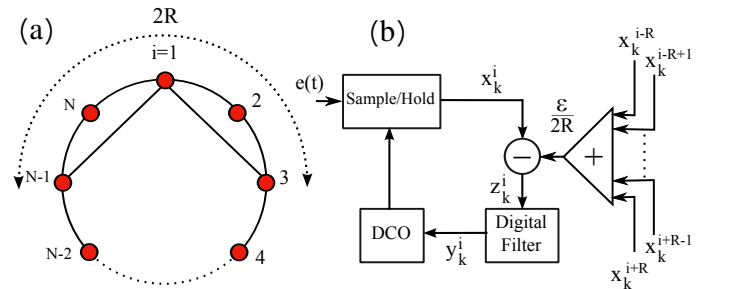


FIG. 2. The schematic architecture of an 1D network of ZC1-DPLLs with nonlocal coupling. (a) the nonlocal coupling scheme with periodic boundary condition. In this figure we draw only the coupling links of  $i = 1^{\text{st}}$  ZC1-DPLL which is coupled with  $R$  ZC1-DPLLs on either side (here  $R = 2$ ). (b) The schematic diagram of the practical circuit realization for the  $i^{\text{th}}$  ZC1-DPLL in the network.  $x_k^i$  is the sampled value of incoming signal for the  $i^{\text{th}}$  ZC1-DPLL at the  $k^{\text{th}}$  sampling instant. Here  $Z_k^i$  is obtained from the difference between  $x_k^i$  and the weighted sum of feedback signals from other nodes of the network.

sites becomes odd, then for  $R = \frac{N-1}{2}$  the feedback term is contributed by all the rest  $N-1$  sites in the lattice and this corresponds to global coupling. But if the total number of sites are even, then the symmetrical coupling up to the entire lattice (global coupling) is not perfectly defined. Thus for  $1 < R < \frac{N-1}{2}$  the feedback is neither local nor global and this case corresponds to nonlocal coupling.

### III. STABILITY ANALYSIS

#### A. Isolated ZC1-DPLL

The steady state phase-error of the isolated system (5) is given by:  $\phi_s = \sin^{-1}\left(\frac{\Lambda_0}{\xi K_1}\right)$ . Stability condition of the isolated ZC1-DPLL can be obtained by using the condition  $|f'(\phi_s)| < 1$ . Where  $f(\phi) = \Lambda_0 + \phi - K_1 \xi \sin(\phi)$  is given by Eq. (5) and  $f'(\phi_s) = 1 - \xi K_1 \cos(\phi_s)$  is the derivative of  $f(\phi)$  at the steady state phase-error  $\phi_s$ . This gives the condition for the stable phase-locked state<sup>29</sup>:  $0 < (K_1 \xi)^2 - \Lambda_0^2 < 4$ . For a phase-step input ( $\xi = 1$ ) the condition reduces to:  $0 < K_1 < 2$ . The system with parameters restricted by this condition settles to the stable steady state or phase-locked condition, which is the required condition for the normal operation of a DPLL. The detailed dynamical behavior of the system (5) was studied in 30. With the variation of loop gain parameter  $K_1$  the system shows a period doubling route to chaos. The bifurcation diagram along with the corresponding Lyapunov exponent spectrum for an isolated ZC1-DPLL is shown in Fig. 3 for  $\xi = 1.1$  (the Lyapunov exponent is given by:  $\lambda = \lim_{n \rightarrow \infty} \frac{1}{n} \sum_{i=1}^n \ln |1 - \xi K_1 \cos(\phi_i)|$ ). Also, the two parameter Lyapunov exponent spectrum in  $K_1 - \epsilon$  space shows the whole scenario of the dynamical features of a ZC1-DPLL<sup>30</sup>.

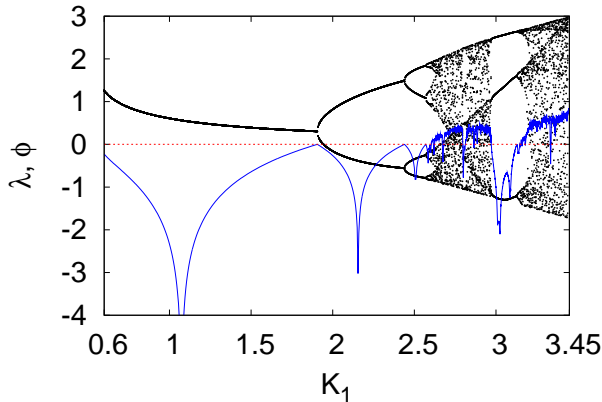


FIG. 3. Bifurcation diagram (black points) along with the Lyapunov exponent spectrum (blue line) of an isolated ZC1-DPLL ( $\xi = 1.1$ ).

#### B. Stability analysis: one-dimensional network of ZC1-DPLLs with nonlocal coupling

The system equation (7) for the one-dimensional network of ZC1-DPLLs with nonlocal coupling is equivalent to a set of  $N$  difference equations. This set of equations can be written as  $\phi_{k+1}^i = J \phi_k^i$ , where  $J$  is the Jacobi matrix of the system. Now for this  $N$  dimensional system the spatial index takes the value in  $i = 1, 2, \dots, N$ . Therefore the Jacobi matrix of the coupled system is given by

$$J = \begin{bmatrix} \frac{\partial \phi_{k+1}^1}{\partial \phi_k^1} & \frac{\partial \phi_{k+1}^1}{\partial \phi_k^2} & \frac{\partial \phi_{k+1}^1}{\partial \phi_k^3} & \dots & \frac{\partial \phi_{k+1}^1}{\partial \phi_k^{N-1}} & \frac{\partial \phi_{k+1}^1}{\partial \phi_k^N} \\ \frac{\partial \phi_{k+1}^2}{\partial \phi_k^1} & \frac{\partial \phi_{k+1}^2}{\partial \phi_k^2} & \frac{\partial \phi_{k+1}^2}{\partial \phi_k^3} & \dots & \frac{\partial \phi_{k+1}^2}{\partial \phi_k^{N-1}} & \frac{\partial \phi_{k+1}^2}{\partial \phi_k^N} \\ \frac{\partial \phi_{k+1}^3}{\partial \phi_k^1} & \frac{\partial \phi_{k+1}^3}{\partial \phi_k^2} & \frac{\partial \phi_{k+1}^3}{\partial \phi_k^3} & \dots & \frac{\partial \phi_{k+1}^3}{\partial \phi_k^{N-1}} & \frac{\partial \phi_{k+1}^3}{\partial \phi_k^N} \\ \vdots & \vdots & \vdots & \vdots & \vdots & \vdots \\ \frac{\partial \phi_{k+1}^N}{\partial \phi_k^1} & \frac{\partial \phi_{k+1}^N}{\partial \phi_k^2} & \frac{\partial \phi_{k+1}^N}{\partial \phi_k^3} & \dots & \frac{\partial \phi_{k+1}^N}{\partial \phi_k^{N-1}} & \frac{\partial \phi_{k+1}^N}{\partial \phi_k^N} \end{bmatrix}. \quad (8)$$

Due to the nonlocal coupling the fixed point of the coupled system becomes

$$\phi_s = \sin^{-1}\left(\frac{\Lambda_0}{K_1 \xi (1 - \epsilon)}\right). \quad (9)$$

The Jacobi matrix (8) of the coupled system at the stable synchronized fixed point can be written as

$$J_s = \begin{pmatrix} a & b & \dots & b & 0 & \dots & 0 & b & \dots & b \\ b & a & b & \dots & b & 0 & \dots & 0 & b & \dots \\ b & b & a & b & \dots & b & 0 & \dots & 0 & b \\ \vdots & \vdots \\ b & \dots & b & 0 & \dots & 0 & b & \dots & b & a \end{pmatrix}. \quad (10)$$

For the symmetrical diffusive coupling  $J_s$  becomes a circulant matrix of order  $(N \times N)$ . It is noteworthy that the first row of the above matrix  $J_s$  has some symmetry as

$$a \quad \underbrace{b \quad \dots \quad b}_{R \text{ terms}} \quad \underbrace{0 \quad \dots \quad 0}_{N - (2R + 1) \text{ terms}} \quad \underbrace{b \quad \dots \quad b}_{R \text{ terms}},$$

that is, it contains one  $a$  term,  $2R$  numbers of  $b$  terms and  $N - (2R + 1)$  terms of 0 (zeros). The next rows can be obtained by shifting the elements to the right side by one unit in each step in the circulant form, where the diagonal terms are

$$a = 1 - \xi K_1 \cos(\phi_s) \quad (11)$$

and the other non-zero off-diagonal terms are

$$b = \frac{\epsilon \xi K_1}{2R} \cos(\phi_s). \quad (12)$$

The stability condition of such dynamical system can be determined by finding the eigenvalues of the Jacobi matrix  $J_s$ . Now,  $J_s$  has  $N$  numbers of eigenvalues,

namely  $\lambda_1, \lambda_2, \dots, \lambda_N$ . Then for the stable synchronized state, absolute of all eigenvalues should be less than unity, i.e.,  $|\lambda_l| < 1$  for all  $l \in [1 : N]$ . This means that the stability constraint is reduced to

$$|\lambda_{max}| < 1, \quad (13)$$

where  $\lambda_{max}$  is the maximum among all the  $N$  eigenvalues. To determine the eigenvalues of  $J_s$  we diagonalize the matrix using Fourier matrix as a diagonalization matrix<sup>31</sup>. A circulant matrix can be diagonalized by using Fourier matrix of the same order. The diagonalized matrix  $U_d$  is obtained by the operation

$$U_d = \frac{1}{N}(F^{-1}J_nF), \quad (14)$$

where  $F$  is the Fourier matrix of order  $N \times N$  whose elements are the independent of the matrix to be diagonalized. The elements of the Fourier matrix are given by  $F_{i,j} = \omega^{(i-1)(j-1)}$ , where  $i$  and  $j$  are respectively the row and column numbers of the respective elements in the matrix and  $\omega$  is the  $N^{th}$  root of unity. Thus Fourier

matrix takes the form as

$$F = \begin{bmatrix} \omega^0 & \omega^0 & \omega^0 & \dots & \omega^0 \\ \omega^0 & \omega^1 & \omega^2 & \dots & \omega^{(N-1)} \\ \omega^0 & \omega^2 & \omega^4 & \dots & \omega^{2(N-1)} \\ \omega^0 & \omega^3 & \omega^6 & \dots & \omega^{3(N-1)} \\ \vdots & \vdots & \vdots & \vdots & \vdots \\ \omega^0 & \omega^{(N-1)} & \omega^{2(N-1)} & \dots & \omega^{(N-1)(N-1)} \end{bmatrix}, \quad (15)$$

and the inverse of the above Fourier matrix is written as

$$F^{-1} = \begin{bmatrix} \omega^0 & \omega^0 & \omega^0 & \dots & \omega^0 \\ \omega^0 & \omega^{-1} & \omega^{-2} & \dots & \omega^{-(N-1)} \\ \omega^0 & \omega^{-2} & \omega^{-4} & \dots & \omega^{-2(N-1)} \\ \omega^0 & \omega^{-3} & \omega^{-6} & \dots & \omega^{-3(N-1)} \\ \vdots & \vdots & \vdots & \vdots & \vdots \\ \omega^0 & \omega^{-(N-1)} & \omega^{-2(N-1)} & \dots & \omega^{-(N-1)(N-1)} \end{bmatrix}. \quad (16)$$

Now, all the eigenvalues  $\lambda_i$  are obtained by finding the diagonal elements of (14). The general analytical expression for the diagonal elements and hence the eigenvalues are found to be

$$\begin{aligned} \lambda_d(l) &= 1 - K_1\xi \cos(\phi_s) + \frac{\epsilon K_1\xi}{R} \cos(\phi_s) \left[ \cos\left(\frac{2\pi}{N}l\right) + \cos\left(\frac{2\pi}{N}2l\right) + \cos\left(\frac{2\pi}{N}3l\right) + \dots + \cos\left(\frac{2\pi}{N}Rl\right) \right] \\ &= 1 - K_1\xi \cos(\phi_s) + \frac{\epsilon K_1\xi}{R} \cos(\phi_s) \sum_{m=1}^R \cos\left(\frac{2\pi}{N}ml\right). \end{aligned} \quad (17)$$

Therefore, the largest eigenvalue among all these can be obtained by putting the values of corresponding  $l$  and other parameters in the above expression. Then we use the condition (13) to determine whether the system is in stable synchronized state or not and find the zone in parameter space to describe the region of synchronization in the same space.

#### IV. RESULTS: ONE-DIMENSIONAL ARRAY

We carry out extensive numerical simulation on the system equation (7) for a system size  $N = 256$ . In all the simulations random initial conditions for phases of each DPLLs are taken: the random numbers are uniformly distributed in the range  $[-\pi, +\pi]$ , which is the possible values of phases  $\{\phi\}$  of ZC1-DPLLs. The value of the normalized incoming frequency for each DPLLs are kept constant at  $\xi = 1.1$ , which is a practical value used in the DPLL literature. In all the simulations 5000 initial time steps discarded to avoid transients.

##### A. Phase diagram

Fig 4 represents the phase diagram showing several spatiotemporal dynamics in the  $K_1 - \epsilon$  parameter space for a fixed coupling range  $R = 105$  (note that this value of  $R$  is far from nearest neighbor coupling  $R = 1$ ). We

map the parametric zone of occurrence of the following prominent dynamical states: (i) Synchronized fixed point (SFP) pattern, where all the DPLLs are phase-locked or synchronized with each other, (ii) pattern selection (PS), where the total network is subdivided into several clusters of standing waves having well characterized wavelengths (to be discussed later), (iii) Frozen random pattern (FRP), where cluster forms but unlike PS there exists no temporal variation of the clusters, (iv) spatiotemporal chaos (STC), where all the DPLLs show chaotic behavior both spatially and temporally, and (ii) Chimera state, i.e., the coexistence of coherence and incoherence. In the phase diagram we also plot the boundary corresponding to the SFP state obtained from the analytical expression of (17) along with (13). It is obvious that the analytical and simulation results agrees well.

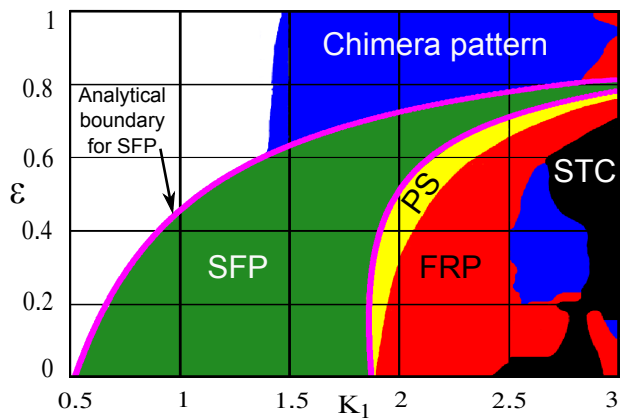


FIG. 4. The phase diagram in the  $K_1 - \epsilon$  parameter space. The region of different dynamics are shown: SFP, FRP, PS, Chimera state and spatiotemporal chaos (STC) for a system size  $N = 256$ , coupling range  $R = 105$  and  $\xi = 1.1$ . The thick (magenta) line around the SFP region gives the stability curve obtained analytically in (17) along with (13): It matches with the numerical results. In the white region there is no distinguished recognizable regular spatiotemporal patterns rather it shows quasiperiodic and chaotic behaviors.

## B. Chimera state

It is seen from the phase diagrams (Fig. 4) that due to nonlocal coupling there is a broad parameter zone where chimera state exists. In Fig.5 we demonstrate the transition from the SFP state (Fig. 5(a)) to the chimera state (Fig. 5(c)) with the variation of coupling strength  $\epsilon$ . In the SFP state (Fig.5(a)) at  $\epsilon = 0.7$  all the DPLLs are synchronized with a constant  $\phi_s = 1.258$  (as predicted analytically in (9)). With an increase in  $\epsilon$  chimera state emerges: it is shown in Fig. 5(c) for  $\epsilon = 0.8$ . Here we can observe the coexistence of coherent and incoherent DPLLs.

To characterize the emergence of the chimera state we use the concept of local curvature proposed recently by Kemeth *et al.*<sup>32</sup>. The *local curvature* in one dimensional systems is defined as the second derivative of the local attributes (phase states) of the network with the space coordinate. It is defined as

$$\begin{aligned} \nabla(\nabla\phi_k^{(i)}) &= \nabla\phi_k^{(i)} - \nabla\phi_k^{(i-1)} \\ &= \{\phi_k^{(i+1)} - \phi_k^{(i)}\} - \{\phi_k^{(i)} - \phi_k^{(i-1)}\} \\ &= \phi_k^{(i+1)} - 2\phi_k^{(i)} + \phi_k^{(i-1)}. \end{aligned} \quad (18)$$

This expression of the local curvature of the phase states characterizes the spatial coherence among the neighbor sites<sup>32</sup>. The local curvature for the SFP and the chimera states are shown in Fig. 5(b) and Fig. 5(d), respectively (at  $K_1 = 2$  and  $R = 105$ ). The local curvature curve shows that for the coherent domain it becomes zero whereas in the incoherent domains it fluctuates randomly with non zero values.

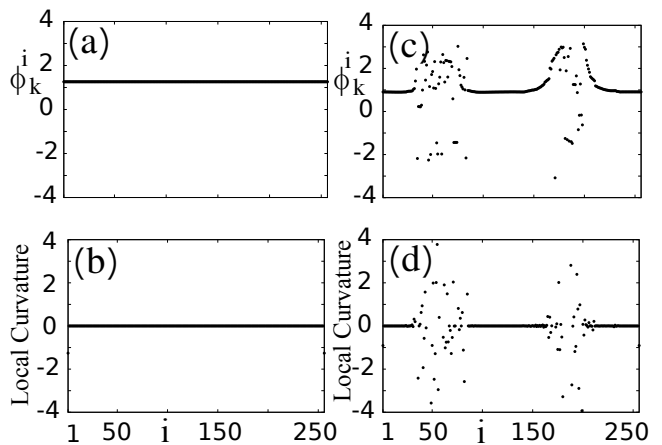


FIG. 5. The transition from synchronized fixed point (SFP) to chimera state with the increase in coupling strength  $\epsilon$ . (a),(b): SFP pattern with  $\epsilon = 0.7$ . (c),(d): chimera pattern with  $\epsilon = 0.8$ . Snapshot of  $\phi_k^i$  (at  $k = 5100$ ) [(a) and (c)] of all the nodes, and the corresponding local curvature given by (18) [(b) and (d)] demonstrate the coexistence of coherent and incoherent states in the chimera state. The local curvature curves show that for the coherent domain it becomes zero whereas in the incoherent domains it fluctuates randomly with non zero values. Other parameters:  $K_1 = 2$  and  $R = 105$ .

To get an idea of the parameter zone of local dynamics (i.e.,  $K_1$ ) where chimera occurs we plot the bifurcation diagram for the coupled network of DPLLs with the variation of gain parameter  $K_1$  [shown in Fig.6 for  $\epsilon = 0.4$  and  $R = 105$ ]. The shaded zone indicates the parametric zone of the gain parameter ( $K_1$ ) where chimera state emerges. This zone of gain parameter is instructive for the choice of  $K_1$  in the search of chimera in the 2D network of DPLLs (discussed in the next section). For other values of  $R$  the qualitative structure of the bifurcation structure remains the same.

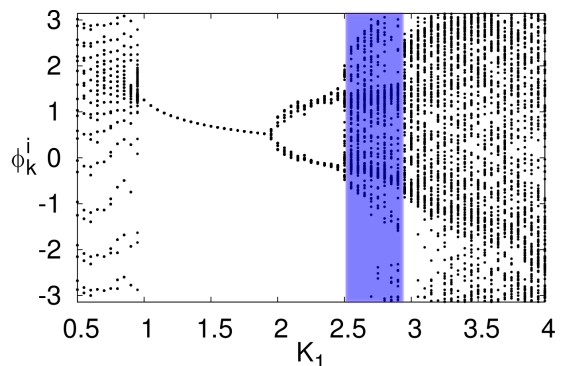


FIG. 6. The bifurcation diagram for the whole network with the variation of gain  $K_1$  ( $R = 105$  and  $\epsilon = 0.4$ ). The shaded zone indicates the parametric zone of occurrence of chimera.

Further, we study how the coupling range  $R$  affects the spatiotemporal patterns. For this we investigate the pat-

tern selection dynamics and its dependence on the coupling range  $R$ : these are shown in Fig. 7(a) and Fig. 7(b), respectively. In the pattern selection state the total lattice dimension is subdivided equally into several domains. The pattern is similar to the formation of standing wave in the system and the dimension of each domain is equal to the wavelength of the formed standing wave. The number of total wavelengths in the whole dimension is called wave numbers. Figure 7(a) shows the standing wave pattern with  $R = 50$  showing eight domains. As coupling range  $R$  increases the number of standing waves decreases: this is shown in the Fig. 7(b). This means that a larger  $R$  prefers the SFP pattern (i.e., zero wave number), therefore, leads to global synchronization. It is expected as larger  $R$  leads to the global coupling, which is known as to support the global synchronization.

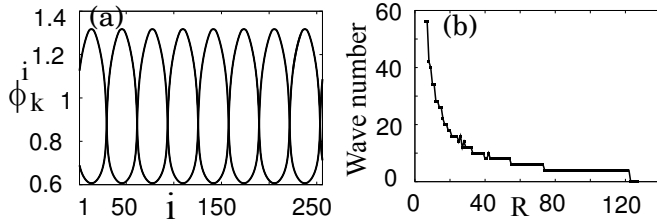


FIG. 7. (a) The pattern selection (for  $R = 50$ ). The spatial domain is subdivided into eight domains; the length of each domain is considered to be the wavelength of the appeared standing wave. (b) The variation of wave number with  $R$ : the wave number decreases exponentially with the increase in  $R$ . Other parameters:  $K_1 = 2.75$ ,  $\epsilon = 0.73$ .

## V. 2D NETWORK: COUPLING SCHEME AND MATHEMATICAL MODEL

We consider a two-dimensional (2D) network of coupled ZC1-DPLLs with orthogonal mesh of dimension  $(N \times N)$  with periodic boundary condition. Figure 8 shows the representative spatial layout of the 2D network with ZC1-DPLLs at each nodes of the mesh. We consider the toroidal boundary condition with nonlocal coupling scheme, i.e., a periodic boundary condition which is compatible with the 2D network structure. Each ZC1-DPLL at the nodes of the network are non-locally coupled with their neighbors that are located within the *circle of influence* whose area is determined by the radial distance from the node in consideration. Therefore, a ZC1-DPLL at the spatial position  $(i, j)$  is coupled with those ZC1-DPLLs that are inside the circle of radius  $R$  (in the unit of lattice constant of the mesh or lattice) centered at the position  $(i, j)$ . Here  $R$  is called the coupling range:  $R = 1$  corresponds to the nearest neighbor coupling whereas  $R = 0$  refers to the condition of no coupling and the system is considered to be an ensemble of isolated  $N^2$  ZC1-DPLLs.

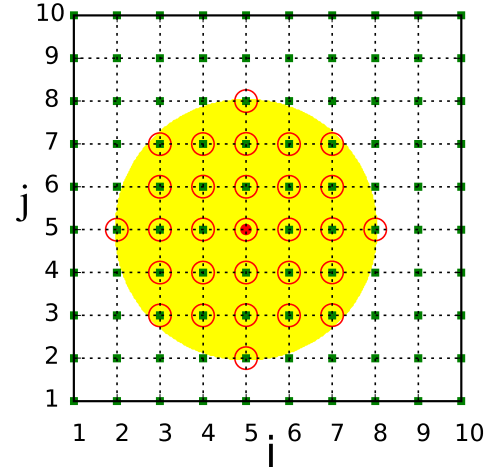


FIG. 8. The representative schematic diagram of the coupling scheme of a 2D network of nonlocally coupled ZC1-DPLLs. We show it for  $N = 10$  and coupling range  $R = 3$ . Each node of the mesh contains a ZC1-DPLL (shown with filled square) coupled with neighboring sites with periodic boundary condition (or toroidal boundary condition). The indices  $i$  and  $j$  represent the spatial co-ordinates in two mutually perpendicular direction of the 2D matrix. The coupling topology is shown for a particular site  $i = j = 5$  (depicted by the red solid circle). The node with  $i = j = 5$  is coupled with those nodes, which fall within the circle of influence (shown with (yellow) shading) with a fixed radial distance. The nodes that are coupled with the  $(i, j) = (5, 5)$ -th site are encircled by red hollow circles.

The system equation of the 2D network of coupled ZC1-DPLLs with nonlocal coupling can be written as (in line of the method used in Sec. II B)

$$\phi_{k+1}^{i,j} = \Lambda_0 + \phi_k^{i,j} - \xi K_1 \sin \phi_k^{i,j} + \frac{\epsilon \xi K_1}{N_R - 1} \sum_{m,n} \left[ \sin(\phi_k^{m,n}) - \sin(\phi_k^{i,j}) \right]. \quad (19)$$

The indices  $i$  and  $j$ , indicating the spatial coordinates in the two mutually perpendicular directions, are bounded in the interval  $i, j \in [1 : N]$  having only integer values. The index  $k$  represents temporal sequences of the evolutions. The indices  $m$  and  $n$  are used to include the effect of the coupling topology. The values of  $m$  and  $n$  for the  $(i, j)$ -th site is such that the coupling is realized within a circular region of radius  $R$  centered at the  $(i, j)$ -th site; Therefore,

$$m, n \in [(m - i)^2 + (n - j)^2 \leq R^2] \quad (20)$$

and

$$N_R = 1 + 4 \sum_{p=0}^{\infty} \left( \lfloor \frac{R^2}{4p+1} \rfloor - \lfloor \frac{R^2}{4p+3} \rfloor \right), \quad (21)$$

where  $N_R$  is the number of ZC1-DPLLs which are coupled to a particular node of the network when the coupling radius is  $R$ . Here  $p$  can take only integer values.

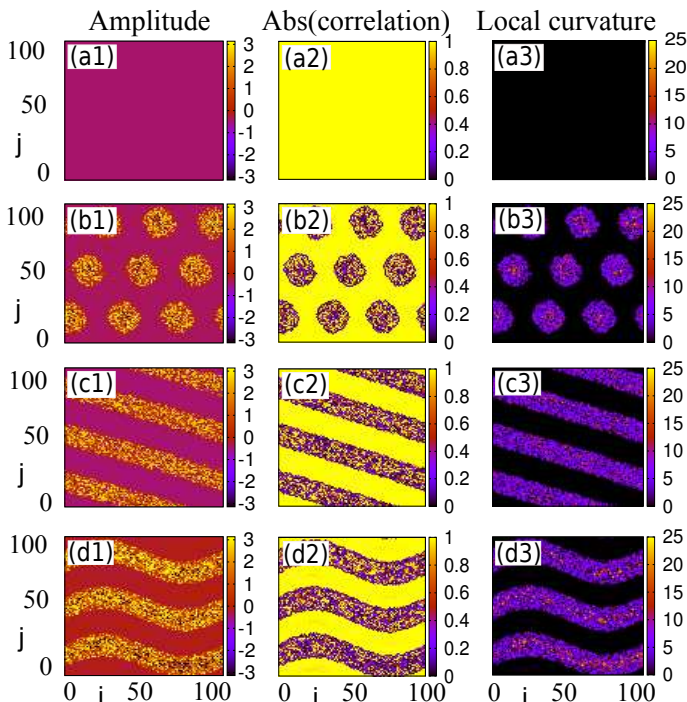


FIG. 9. (a1)–(d1) Amplitude plots; (a2)–(d2) Respective plots of the absolute values of the local correlation coefficient and (a3)–(d3) Respective local curvatures. The figure shows the transition from SFP (a1-a3) for  $\epsilon = 0.2$  → grid chimera (b1-b3) for  $\epsilon = 0.3$  → striped chimera (c1-c3) for  $\epsilon = 0.4$  → wavy strip chimera (d1-d3) for  $\epsilon = 0.5$ . Here  $K_1 = 2.75$ ,  $R = 25$  are kept constant.

For example, from Fig. 8 it is the number of ZC1-DPLLs within the yellow shaded region; in this case  $N_R = 29$  (including the red circle) with  $R = 3$ . The symbol  $\lfloor \cdot \rfloor$ , is called the floor function, produces the largest integer less than or equal to its argument.

## VI. RESULTS

Numerical simulations are carried out on the 2D-network of  $(100 \times 100)$  sites with toroidal boundary conditions. In all the simulations we consider random initial conditions uniformly distributed in the range  $[-\pi, +\pi]$ , which is the natural range of values of phase-errors ( $\phi$ ) for a DPLLs. Also, the normalized frequency of the incoming signals to each DPLL in the network is kept at a physically realistic value  $\xi = 1.1$ . To discard the transients, all the spatiotemporal plots are presented after  $k = 5000$ .

Our simulation results reveal that there exist several 2D spatiotemporal patterns, which can be broadly classified in to two categories, namely chimera patterns and non-chimera patterns. The typically observed chimera patterns are grid chimera or spot chimera, Stripped chimera and wavy strips chimera. Figures 9(a1)–(d1)

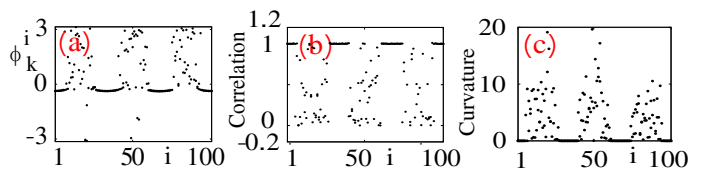


FIG. 10. The cross sectional view of Figs. 9(b1)–(b3) along  $i = 50$ . (a) Spatial variation of amplitude of local attribute (phase angle), (b) absolute value of local correlation coefficient (c) the local curvature  $D$  for the fixed  $j = 50$  with the variation of index  $i$ . Parameter values are:  $R = 25$ ,  $\epsilon = 0.3$ ,  $K_1 = 2.75$  and  $L = 1$

show the transition from the synchronized fixed point (SFP) pattern to several chimera patterns with the increase of coupling strength ( $\epsilon$ ) for a fixed coupling range  $R = 25$  (here  $K_1 = 2.75$ ). Figure 9(a1) shows the SFP state for  $\epsilon = 0.2$ : in this state all the DPLLs are phase-locked with each other and this is the normal (or desirable) condition of operation. With an increase in  $\epsilon$  *grid chimera* pattern appears. This is shown in Fig. 9(b1) for  $\epsilon = 0.3$ : here incoherent spots emerge in the background of synchronized pattern. Later in this paper we will see that the diameter of these spots depends upon the coupling range  $R$ . Further increase of  $\epsilon$  results in *stripped chimera* pattern as shown in Fig. 9(c1) for  $\epsilon = 0.4$ : we see that in this chimera state the incoherent domains are exhibiting strips of certain width (we will see that the width of the strip increases with  $R$ ). Finally, for a larger value of  $\epsilon$  we get *wavy strip* chimera patterns (Figure 9(d1) for  $\epsilon = 0.5$ ): here, interestingly, the incoherent domains (and thus the coherent domains) show a wave like pattern. For a better understanding of the coherent-incoherent structure of the chimera pattern we show the cross section of Fig. 9(b1) along  $j = 50$  in Fig. 10(a1): one can see three incoherent regions corresponding to the three incoherent spots of Fig. 9(b1).

To ensure the occurrence of chimera patterns we introduce two quantifiers that measures the spatial correlation among the different sites, namely the local correlation coefficient<sup>8,33</sup> and the local curvature<sup>32</sup>. Both these measures provide the degree of coherence among the nodes and therefore are capable of distinguishing coherent and incoherent domains. The local correlation coefficient is defined as<sup>33</sup>,

$$(e_k^{i,j})_L = \frac{\sum_{m',n'} \hat{\phi}_k^{i,j} \hat{\phi}_k^{m',n'}}{\sum_{m',n'} (\hat{\phi}_k^{m',n'})^2} \quad (22)$$

Where  $m', n'$  refers to the sites that are within a circle of radius of  $L$  centered at the site having index  $(i, j)$ . So,

$$m', n' \in (m' - i)^2 + (n' - j)^2 \leq L^2 \quad (23)$$

$L$  is called the degree of correlation. For first order (local) correlation,  $L = 1$ , the correlation is totally with the nearest neighbors; whereas for second order,  $L = 2$ , includes the second nearest neighbours and so on. Now as

before,

$$N_L = 1 + 4 \sum_{p=0}^{\infty} \left\{ \left\lfloor \frac{L^2}{4p+1} \right\rfloor - \left\lfloor \frac{L^2}{4p+3} \right\rfloor \right\}. \quad (24)$$

The deviation of phases of the ZC1-DPLLs in the equation (22) are follows:

$$\hat{\phi}_k^{i,j} = \phi_k^{i,j} - \langle \phi_R^{i,j} \rangle_k, \quad (25)$$

is the deviation of phase of the  $(i, j)$ -th site.

$$\hat{\phi}_k^{m',n'} = \phi_k^{m',n'} - \langle \phi_R^{i,j} \rangle_k \quad (26)$$

is the deviation of phases of those sites that are within the range of order of correlation. For local correlation this range is a unit circle centred at  $(i, j)$ -th. Here  $\langle \phi_R^{i,j} \rangle_k$  is the average of the local phases up-to the coupling range  $R$  of the system for the spatial index  $(i, j)$  and is given by

$$\langle \phi_R^{i,j} \rangle_k = \frac{1}{N_R} \sum_{m,n} \phi_k^{m,n} \quad (27)$$

Where  $m, n$  and  $N_R$  are given in Eqns. (20) and (21) respectively. The value of the local correlation co-efficient  $\text{abs} \left( (e_k^{i,j})_L \right) = 1$  corresponds to the local synchronization, and the deviation of the value from unity means local incoherence.

Next we use the local curvature<sup>32</sup> quantified by the general Laplacian of the phase distribution or amplitude distribution (for a fixed time, i.e., snapshot of phases or amplitudes) of the spatially distributed oscillators (note that for 1D case, the general Laplacian is simply a second derivative as used in (18)). For the two-dimensional case the second order difference equation becomes

$$\begin{aligned} D &= \nabla(\nabla \phi_k^{(i,j)}) = \nabla_i^2 \phi_k^{(i,j)} - \nabla_j^2 \phi_k^{(i,j)} \\ &= \phi_k^{(i+1,j)} + \phi_k^{(i-1,j)} + \phi_k^{(i,j+1)} + \phi_k^{(i,j-1)} \\ &\quad - 4\phi_k^{(i,j)}, \end{aligned} \quad (28)$$

which is symmetric with respect to the center element  $\phi_k^{(i,j)}$  in two-dimensional space. The equations (28) represents the local curvature  $D$  in two-dimensional space. The value of  $D = 0$  corresponds to the coherent and non-zero values refers to the incoherent domains. These two measures are shown in Figs. 9 to support our results: the middle column [Figs. 9(a2)–(d2)] represents the absolute value of the local correlation coefficient and the right most column [Figs. 9(a3)–(d3)] shows the local curvature  $D$ . In Figs. 9 (a2)–(d2) the coherent nodes have the (absolute) local correlation coefficient equal to unity [shown in light gray (yellow) shading], whereas the incoherent nodes differ from unity [see the color map in Figs. 9(a2)–(d2)]. Equivalently, in Figs. 9(a3)–(d3) the local curvature  $D$  for the coherent nodes is zero (shown by black shading) and that for incoherent domains are

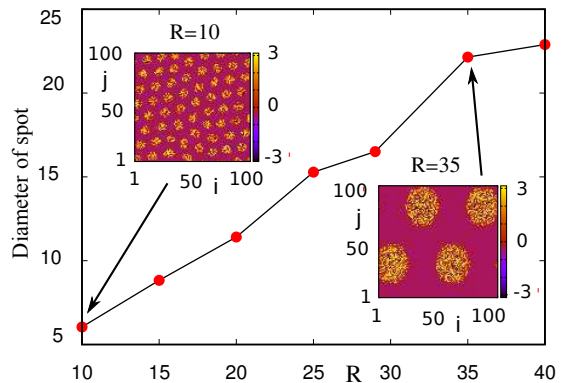


FIG. 11. Variation of diameter of circular incoherent spots with the range of coupling  $R$  for fixed  $\epsilon = 0.3$  and  $K_1 = 2.75$ .

nonzero. In Fig. 10(b) and Fig. 10(c) represent this scenario clearly for the grid chimera: in the incoherent zones the local correlation coefficient attains a value less than unity whereas the local curvature  $D$  jumps from its zero value (for coherent nodes) to larger nonzero values.

Next we investigate the dimension of incoherent regions in the case of grid and strip chimeras. We find that in the case of grid chimera, the dimension of the incoherent spot increases with the range of the coupling  $R$ . The diameter of a grid is measured as the fractional percentage with respect to the dimension of 2D space lattice. Therefore, the number of incoherent spots decreases with an increase in  $R$ . This is shown in Fig. 11 ( $\epsilon = 0.3$ ,  $K_1 = 2.75$ ): two representative patterns of the grid chimera for  $R = 10$  and  $R = 35$  are also shown in the inset showing the increasing spot size with  $R$ . In the case of the strip chimera the width of the incoherent strips (therefore, also, that of the coherent strips) increases with  $R$ . The width of the strips are measured as the fractional percentage with respect to the dimension of diagonal length of the total 2D space lattice. This is shown in Fig. 12 ( $\epsilon = 0.6$ ,  $K_1 = 2.75$ ): it can be seen that the width of the incoherent strips increases monotonically obeying a quadratic polynomial function (obtained by numerically fitting the data). Also shown are two representative strip chimera patterns for  $R = 30$  and  $R = 49$ . Interestingly, we observed that the dimension of spots or the width of the strips are independent of the variation of value of coupling parameter  $\epsilon$  and the gain constant  $K_1$ .

As discussed in the beginning of this section, apart from chimera patterns we also observed other non-chimera spatiotemporal patterns, namely spatially irregular period-two [Fig. 13(a)], spatially multiple periodic [Fig. 13(b)] and spatial chaos [Fig. 13(c)] patterns for different choice of  $R$ ,  $\epsilon$  and  $K_1$ . These regular non-chimera patterns are shown in the Fig. 13. The phase diagram of the parametric zone of occurrence of chimera patterns with respect to the non-chimera pattern is shown in Fig. 14 in the  $\epsilon - R$  space at a fixed value of  $K_1$ .

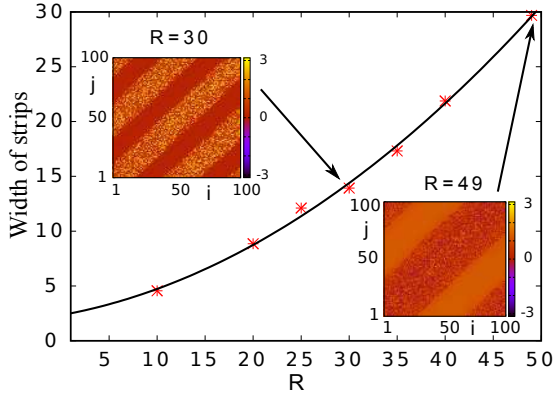


FIG. 12. Variation of incoherent strip width with the coupling range  $R$  (shown in points) for fixed  $\epsilon = 0.6$  and  $K_1 = 2.75$ . The curve is fitted with the polynomial  $ax^2 + bx + c$ , where  $a = 0.008128$ ,  $b = 0.1579$  and  $c = 2.338$  (solid line).

Black squares represent non-chimera states whereas gray (red) and light gray (yellow) squares represent grid and stripe (linear and wavy) chimera patterns, respectively. It is noteworthy that at much lower value of  $\epsilon$  chimera patterns do not appear.

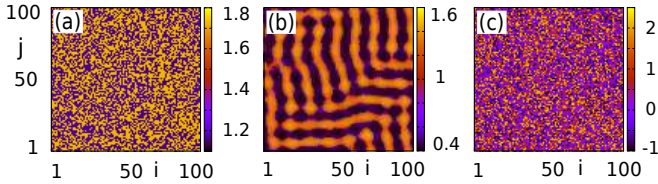


FIG. 13. Non-chimera patterns: (a) spatially irregular period-two pattern ( $R = 10$ ,  $\epsilon = 0.10$ ,  $K_1 = 2.75$ ), (b) spatial multiple periodic solutions ( $R = 10$ ,  $\epsilon = 0.70$ ,  $K_1 = 2.70$ ), and (c) spatial chaos ( $R = 20$ ,  $\epsilon = 0.10$ ,  $K_1 = 2.75$ ).

## VII. CONCLUSION

In this paper we have studied 1D and 2D array of DPLLs with nonlocal coupling and shown that a network of DPLLs may show spatiotemporal instability like chimera states even in its normal coupling condition. For the 1D network of nonlocally coupled DPLLs we have carried out a linear stability analysis to identify the zone of normal operation of DPLLs, i.e., the zone of stable synchronized state. For the 2D array we have demonstrated that outside the zone of globally synchronized state several chimera patterns, such as strip and spot chimera emerge. With suitable measures like local curvature and correlation coefficient we have characterized the occurrence of the chimera patterns.

Note that, in this paper our goal is not to *wishfully* design a set up under which chimeras emerge, but, contrary to most of the studies, we show that a real engineer-

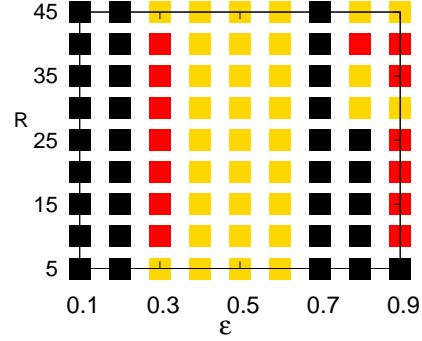


FIG. 14. The phase diagram representing different spatial patterns in the  $R - \epsilon$  parameter space (for a fixed  $K_1 = 2.75$ ). Color code: Black represents non-chimera patterns, Red represents grid chimera pattern, and Yellow is for stripe (linear or wavy) chimera patterns.

ing system even under its *normal coupling condition* may show chimera patterns. From technical point of view, our study clearly set a road map for a designer to choose the coupling and system parameters such that the network operates in its normal (i.e., phase-locked) condition. Further, in the context of control, this study reveals that only bifurcation and chaos control in DPLLs are not sufficient to ensure its normal operating condition, but in a network of DPLLs effective control schemes have to be implemented to tame chimera and other spatiotemporal states. Finally, our study also offers a natural system architecture where one can experimentally realize chimeras: since DPLLs are implemented using the low cost FPGA and DSP boards, therefore, the experimental observation of chimeras would be much easier. Moreover, the occurrence of chimeras in DPLLs may arouse the attention of researchers to explore the possibility of exploiting chimeras in electronic communication and signal processing systems.

## ACKNOWLEDGMENTS

Authors convey their sincere thanks to Prof. B. C. Sarkar for introducing them to the field of phaselock techniques. T.B. acknowledges the fruitful discussion with Prof. Eckehard Schöll at TU-Berlin during his visit supported by DFG in the framework of SFB 910.

<sup>1</sup>F. M. Gardner, *Phaselock Techniques*, 2nd ed. (Wiley, New york, 1979).  
<sup>2</sup>G. A. Leonov and N. V. Kuznetsov, *Nonlinear Mathematical Models of Phase-Locked Loops. Stability and Oscillations*, Vol. 7 (Cambridge Scientific Publisher, 2014) ISBN 978-1-908106-38-4.  
<sup>3</sup>M. Zoltowski, *Signal Processing*, **81**, 735 (2001).  
<sup>4</sup>G. A. Leonov, N. V. Kuznetsov, and S. M. Seledzhi, “Automation control– theory and practice,” (In-Tech, 2009) Chap. Non-linear Analysis and Design of Phase-Locked Loops, pp. 89–114.

- <sup>5</sup>G. A. Leonov and S. M. Seledzhi, *Int. J. Bifurcation and Chaos* **15**, 1347 (2005).
- <sup>6</sup>M. de Sousa Vieira, A. J. Lichtenberg, and M. A. Lieberman, *Int. J. Bifurcation Chaos* **1**, 691 (1994); W. E. Wonchoba, M. A. Lieberman, and A. J. Lichtenberg, *Nonlinearity* **7**, 1695 (1994).
- <sup>7</sup>G. Goldsztein and S. Strogatz, *Int. J. of Bifurcations Chaos* **5**, 983 (1995).
- <sup>8</sup>T. Banerjee, B. Paul, and B. C. Sarkar, *Chaos* **24**, 013116 (2014).
- <sup>9</sup>B. Paul, T. Banerjee, and B. C. Sarkar, *International Journal of Bifurcation and Chaos* **26**, 1650076 (2016).
- <sup>10</sup>Y. Kuramoto and D. Battogtokh, *Nonlinear Phenomena in Complex Systems* **5**, 380 (2002).
- <sup>11</sup>M. J. Panaggio and D. M. Abrams, *Nonlinearity* **28**, R67 (2015).
- <sup>12</sup>E. Schöll, *Eur. Phys. J. Special Topics* **225**, 891 (2016).
- <sup>13</sup>A. Schmidt, T. Kasimatis, J. Hizanidis, A. Provata, and P. Hövel, *Phys. Rev. E* **95**, 032224 (2017).
- <sup>14</sup>C.-H. Tian, X.-Y. Zhang, Z.-H. Wang, and Z.-H. Liu, *Frontiers of Physics* **12**, 128904 (2017).
- <sup>15</sup>T. Kasimatis, J. Hizanidis, and A. Provata, *Phys. Rev. E* **97**, 052213 (2018).
- <sup>16</sup>N. C. Rattenborg, C. J. Amlaner, and S. L. Lima, *Neurosci Biobehav Rev.* **24**, 817 (2000).
- <sup>17</sup>N. C. Rattenborg, *Naturwissenschaften* **93**, 413 (2006).
- <sup>18</sup>A. M. Hagerstrom, T. E. Murphy, R. Roy, P. Hövel, I. Omelchenko, and E. Schöll, *Nature Physics* **8**, 658 (2012).
- <sup>19</sup>M. R. Tinsley, S. Nkomo, and K. Showalter, *Nat. Phys.* **8**, 662 (2012).
- <sup>20</sup>J. F. Tetz, J. Rode, M. R. Tinsley, K. Showalter, and H. Engel, *Nature Physics* **14**, 282 (2018).
- <sup>21</sup>L. Larger, B. Penkovsky, and Y. Maistrenko, *Nature Communications* **6**, 7752 (2015).
- <sup>22</sup>K. T, K. P, W. J, C. K, and M. Y, *Scientific Reports* **4** (2014).
- <sup>23</sup>E. A. Martens, S. Thutupalli, A. Fourriere, and O. Hallatschek, *Proceedings of the National Academy of Sciences* **110**, 10563 (2013).
- <sup>24</sup>A. E. Motter, S. A. Myers, M. Anghel, and T. Nishikawa, *Nature Physics* **9**, 1745 (2013).
- <sup>25</sup>J. C. González-Avella, M. G. Cosenza, and M. San Miguel, *Physica A: Statistical Mechanics and its Applications* **399**, 24 (2014).
- <sup>26</sup>J. Hizanidis, N. Lazarides, and G. Tsironis, *Phys. Rev. E* **94**, 032219 (2016).
- <sup>27</sup>T. Banerjee and B. C. Sarkar, *Signal Processing* **85**, 1611 (2005).
- <sup>28</sup>W. C. Lindsey and C. M. Chie, *Proceedings of IEEE* **69**, 410 (1981).
- <sup>29</sup>H. C. Osborne, *Communications, IEEE Transactions on* **28**, 1343 (1980).
- <sup>30</sup>T. Banerjee and B. C. Sarkar, *Int. J of Bifurcation and Chaos* **22**, 1230044 (2012).
- <sup>31</sup>P. M. Gade, *Phys. Rev. E.* **57**, 14897 (1998).
- <sup>32</sup>F. P. Kemeth, S. W. Haugland, L. Schmidt, I. G. Kevrekidis, and K. Krischer, *Chaos: An Interdisciplinary Journal of Nonlinear Science* **26**, 094815 (2016).
- <sup>33</sup>D. B. Vasconcelos, R. L. Viana, S. R. Lopes, A. M. Batista, and S. E. de S. Pinto, *Physica A* **343**, 201 (2004).